TRAMAT 2 (2026) 100206

Contents lists available at ScienceDirect

Transactions of Materials Research

journal homepage: www.sciencedirect.com/journal/transactions-of-materials-research

Autogenous Al_2O_3-rich passive film confers exceptional corrosion resistance to Ti_3AlC_2 coating in 3.5 wt.% NaCl solution

Yuxi Xu [a,b], Qizhen He [a], Guanshui Ma [a], Zhenyu Wang [a], Kaihang Wang [a], Yiqun Feng [a], Aiying Wang [a,b,*]

[a] State Key Laboratory of Advanced Marine Materials, Zhejiang Key Laboratory of Extreme-environmental Material Surfaces and Interfaces, Ningbo Institute of Materials Technology and Engineering, Chinese Academy of Sciences, Ningbo, 315201, China
[b] College of Materials Science and Opto-Electronic Technology, University of Chinese Academy of Sciences, Beijing, 100049, China

ARTICLE INFO

Keywords:
MAX phase
Ti_3AlC_2 coating
Electrochemical corrosion
Passive film
Growth kinetics

ABSTRACT

This study investigates the electrochemical corrosion behavior and surface passive mechanism of Ti_3AlC_2 MAX phase coating to advance their application in marine environments. Ti_3AlC_2 coating was deposited on a Ti-6Al-4V substrate using high-power impulse magnetron sputtering followed by annealing, and its corrosion performance was systematically evaluated in 3.5 wt.% NaCl solution. The results revealed exceptional corrosion resistance with a current density of 5.74×10^{-10} A•cm^{-2}, which is two orders of magnitude lower than that of the substrate, along with higher impedance modulus, demonstrating superior corrosion resistance. Microscopic characterization confirmed the formation of a continuous, dense, amorphous Al_2O_3 passive film with an average thickness of 4.07 nm. The lower vacancy formation energy of Al atoms, as determined by DFT calculations, underpins the preferential diffusion of Al in Ti_3AlC_2 and accounts for the formation of a single Al_2O_3 passivation layer at the microscopic scale. The film growth follows a high-field model, with thickness increasing logarithmically over time, governed by inward oxygen ion migration. Critically, the relatively low aluminum content in Ti_3AlC_2 leads to form an amorphous diffusion transition zone beneath the passive film. This diffusion zone mitigates structural destabilization caused by aluminum depletion, preventing film delamination and enhancing long-term protection. The study elucidates the selective formation and growth mechanisms of the passive film on Ti_3AlC_2 MAX phase coating, providing a theoretical basis for their use in aggressive corrosive environments.

1. Introduction

In marine environments, offshore service equipment faces severe electrochemical corrosion due to prolonged exposure to salty, humid atmospheric conditions and chloride-rich salt deposition, significantly limiting its service life and safety [1–3]. Surface coating technology, which applies functional layers onto substrates, offers an advanced approach to enhance material performance. Thus, developing novel protective coatings that combine high-temperature stability with superior corrosion resistance is of considerable engineering and scientific relevance. MAX phases, a class of thermodynamically stable ceramics with metallic properties, are represented by the general formula $M_{n+1}AX_n$ ($n = 1$-4), where M is a transition metal such as Ti or Cr, A is an element from groups IIIA/IVA such as Al or Si, and X is C or N [4,5]. These materials possess a hexagonal layered structure with strong covalent bonding between M and X atoms and weaker metallic bonding between M and A atoms [6,7]. The unique bonding arrangement and layered architecture endow MAX phases with a combination of metallic and ceramic properties, including high elastic modulus and hardness, good electrical and thermal conductivity, machinability, excellent oxidation and thermal shock resistance, as well as corrosion resistance [8–12]. These properties render MAX phase coatings a promising candidate for protective applications in demanding environments.

In recent years, the research on corrosion protection properties of MAX phase materials has been extensively investigated. According to the research of Xu et al. [13], Cr_2AlC coating with a $(11\bar{2}0)$ preferred orientation exhibited superior corrosion resistance in a thermal-salt-steam environment at 600 °C, due to enhanced Al diffusion that promoted the formation of a dense Al_2O_3 layer while effectively suppressing Cr_2AlC decomposition. Under electrochemical corrosion,

---

[*] Corresponding author. State Key Laboratory of Advanced Marine Materials, Zhejiang Key Laboratory of Extreme-environmental Material Surfaces and Interfaces, Ningbo Institute of Materials Technology and Engineering, Chinese Academy of Sciences, Ningbo, 315201, China.

E-mail address: aywang@nimte.ac.cn (A. Wang).

https://doi.org/10.1016/j.tramat.2026.100206
Received 11 February 2026; Received in revised form 28 February 2026; Accepted 9 March 2026

(103) oriented Cr_2AlC coating also formed a compact oxide layer, achieving a corrosion current density as low as 2×10^{-2} μA•cm^{-2} [14]. Furthermore, Zhang et al. reported that (Cr, Mo)$_2$AlC MAX phase coating significantly improved corrosion resistance by reducing the formation energy of Al vacancies, thereby accelerating Al transport and promoting the growth of an Al-oxide passive film [15]. A Ti_3SiC_2 coating fabricated via atmospheric plasma spraying on 316L stainless steel exhibited an open circuit potential (OCP) of 162.5 mV, a corrosion current density of 1.72×10^{-6} A•cm^{-2}, and an interfacial contact resistance of 5.49 mΩ•cm^2, indicating promising electrochemical performance [16]. However, despite providing fast diffusion channels for Si atoms, the layered structure of Ti_3SiC_2 exhibits limited passive efficiency at the barrier layer. Thus, its corrosion resistance under open circuit conditions shows no clear advantage over pure Ti, with inferior passive capability [17]. In contrast, Ti_2AlC coating exhibits significantly higher Al mobility than Ti, along with high tolerance to Al vacancy concentrations exceeding 50%, enabling the formation of a dense Al_2O_3 passive film while maintaining structural stability [18]. Collectively, these findings highlight the superior corrosion resistance potential of Al-containing MAX phase materials.

Ti_3AlC_2, a representative Al-containing MAX phase ceramic, exhibits superior fracture toughness compared to lower-order Ti_2AlC, with enhanced toughness at elevated temperatures [19–21], positioning it as a promising material for demanding applications. Studies on composite coatings highlight its corrosion-resistance benefits. Ni60-Ti_3AlC_2 coatings with 12% Ti_3AlC_2 addition achieved optimal salt-fog resistance due to the formation of a dense α-Al_2O_3/TiO_2 bilayer that effectively impedes electrolyte penetration [22]. Similarly, in Co08-$x$$Ti_3AlC_2$ systems, a 15% Ti_3AlC_2 content not only reduced friction and wear but also improved corrosion resistance through the formation of protective corrosion products [23]. While Ti_3AlC_2 maintains low corrosion current densities under simulated proton exchange membrane fuel cells conditions, its electrochemical behavior is environment-dependent [24]. In 3.5% NaCl solution, it displays distinct passive and corrosion resistance, though with limited passive efficiency [25,26]. In 1 M NaOH, a compact bilayer titanium oxide passive film confers excellent corrosion resistance, whereas in 1 M H_2SO_4, intergranular corrosion leads to significant degradation of long-term stability [27].

Despite extensive investigation of Ti_3AlC_2 materials, prior research has predominantly focused on bulk properties, leaving the composition, microstructure, and growth kinetics of the corrosion-induced passive film poorly understood. To address this gap, the dense Ti_3AlC_2 coatings were deposited on Ti-6Al-4V substrates via high-power impulse magnetron sputtering (HiPIMS). While the baseline corrosion resistance of Ti_3AlC_2 in NaCl media is established [25,26], the fundamental nature of the passivation film governing this performance remains elusive, including its spontaneous formation mechanism, nano-structure characteristics, and dynamic growth kinetics under anodic polarization. By integrating systematic electrochemical measurements, microstructural characterization, and density functional theory (DFT) calculations, this study interrogate the corrosion behavior and passivation mechanism of Ti_3AlC_2 coatings in 3.5 wt.% NaCl solution. The work focuses on quantifying the composition, thickness, and structure of passive film; resolving its dynamic growth under anodic conditions; and uncovering the underlying growth mechanism through experiment-theory synergy, aiming to clarify the electrochemical corrosion mechanisms in simulated marine environments.

2. Experimental details

2.1. Coating preparation

Ti-Al-C coatings were deposited on Ti-6Al-4V substrates via high-power impulse magnetron sputtering (HiPIMS) using a TiAl composite target (99.99% purity, Ti:Al = 2:1.3 at.%). Substrates ($30 \times 10 \times 2.5$ mm^3) were mechanically polished to a mirror finish using SiC abrasive papers, followed by ultrasonic cleaning in acetone and ethanol and subsequent drying. Prior to deposition, the chamber was evacuated to below 2×10^{-3} Pa. Substrate surfaces were then etched by Ar plasma under a bias voltage of −200 V to remove contaminants and enhance coating adhesion. To improve interfacial bonding and suppress upward diffusion of substrate elements, a Ti-Al interlayer was first deposited. The Ti-Al-C coating was subsequently grown using Ar and CH_4 as working gases, with flow rates of 200 and 7.5 sccm, respectively. The TiAl target was sputtered at 2000 W with a duty cycle of 5%. Deposition was carried out at 100 °C without external substrate bias. Finally, the as-deposited coating was annealed at 700 °C under vacuum to promote the formation of a Ti_3AlC_2 MAX phase structure. Detailed process parameters have been reported in our previous work [28].

2.2. Electrochemical measurements

Electrochemical corrosion tests were conducted in a 3.5 wt.% NaCl solution using a standard three-electrode configuration with a Gamry Reference 600+ potentiostat. The working electrode was the coated specimen with an exposed area of 0.2 cm^2, a platinum sheet served as the counter electrode, and an Ag/AgCl electrode was used as the reference. The testing protocol comprised the following sequence. First, the open circuit potential (OCP) was monitored for 5 min. Subsequently, a cathodic polarization at −0.8 V (vs. OCP) was applied for 5 min to remove the native oxide layer and ensure a consistent initial surface state. The sample was then immersed for 120 min to obtain a stable OCP, which served as the baseline for subsequent measurements. Electrochemical impedance spectroscopy (EIS) was performed at the stabilized OCP over a frequency range of 10^5 to 10^{-2} Hz with a 10 mV AC amplitude; the data were fitted to equivalent circuits using ZSimpwin software. Potentiodynamic polarization was carried out at a scan rate of 1 mV•s^{-1} from −0.5 V to +1.5 V relative to the stable OCP. Based on the anodic characteristics of the polarization curve, three potentials (0.5 V, 0.8 V, and 1.0 V vs. E_{OCP}) were selected for 10 h potentiostatic polarization to promote passive film formation. After polarization, Mott-Schottky analysis was performed on the passivated samples using a step-wise potential scan from high to low potentials in 100 mV steps at a fixed frequency of 100 Hz. To systematically investigate the dynamic evolution of the passive film, successive EIS measurements were conducted every 30 min during an additional 10 h anodic polarization at 0.5 V.

2.3. Microstructure characterization

The microstructure, chemical composition, and surface state of the as-prepared coatings were systematically characterized using multiple analytical techniques. Phase composition and crystal structure were determined by X-ray diffraction (XRD, D8 Advance, Bruker). Surface morphology and elemental distribution were examined using a field-emission scanning electron microscope (SEM, Sigma 300, Zeiss) equipped with an energy-dispersive X-ray spectrometer (EDS, Oxford Instruments). Chemical states and elemental concentrations within the passivated surface region were analyzed by X-ray photoelectron spectroscopy (XPS, Axis Ultra DLD, Kratos) with a monochromatic Al Kα source. To probe the fine structure and interfacial characteristics of the passive film, cross-sectional transmission electron microscopy (TEM) specimens were prepared via focused ion beam (FIB, Auriga, Carl Zeiss) milling and subsequently examined using high-resolution TEM (Talos F200×, Thermo Fisher).

2.4. Atomic-scale calculations

All calculations were performed using the Vienna Ab initio Simulation Package (VASP) [29], a plane-wave-based density functional theory (DFT) code, employing the projector augmented wave (PAW) method [30]. The exchange-correlation functional was described within the generalized gradient approximation (GGA) using the Perdew-Burke-Ernzerhof (PBE) parametrization [31]. A plane-wave kinetic energy cutoff of 500 eV was adopted to expand the electronic wavefunctions. The Brillouin zone was sampled using a Monkhorst-Pack [32] k-point mesh of 5 × 5 × 1 for the primitive cell. To simulate structural evolution and defect formation in Ti_3AlC_2, a 2 × 2 × 1 supercell containing 32 atoms was constructed. Vacancy defect models were generated by removing specific atoms from the pristine supercell. The vacancy formation energy can be calculated by the following formula:

$$\Delta E_V = E_{def} - E_{per} + \mu_i \tag{1}$$

Here, ΔE_V denotes the energy required to form a single vacancy. E_{def} and E_{per} represent the total energies of the supercell containing a single vacancy and the pristine supercell without any vacancies, respectively. The term μ_i corresponds to the chemical potential of the element, which is highly dependent on the crystal growth environment. In defect formation energy calculations, the chemical potential is typically referenced to the average energy per atom of the element in its ground-state bulk phase [33].

3. Results and discussion

3.1. Microstructure of the prepared Ti_3AlC_2 coatings

Fig. 1 systematically characterizes the phase composition and microstructure of the as-prepared Ti_3AlC_2 coating. In the XRD pattern (Fig. 1a), characteristic diffraction peaks appear at 2θ values of 34.1°, 36.9°, 39.1°, 41.9°, 44.8°, 60.4°, and 74.2°. These correspond precisely to the (101), (103), (104), (105), (106), (110), and (118) planes of the standard Ti_3AlC_2 phase (ICDD PDF#52-0875). The intense and narrow (104) peak indicates high crystallinity of the coating. Apart from diffraction signals from the substrate and minor $TiAl_x$ impurity peaks arising from crystallization of the Ti-Al interlayer during annealing, the XRD data confirm the successful synthesis of a high-purity coating predominantly composed of single-phase Ti_3AlC_2 via HiPIMS followed by annealing. SEM surface analysis (Fig. 1b) reveals a uniform and dense microstructure free of macroscopic defects such as cracks or pores. The morphology exhibits the characteristic nanoscale spherical aggregates typical of magnetron-sputtered coating. EDS within the selected area yields a Ti:Al:C atomic ratio of 47.97:22.56:29.47, close to the theoretical stoichiometry of Ti_3AlC_2. The slightly elevated Al content may originate from interdiffusion within the transition layer during annealing. Cross-sectional TEM further corroborates the structural integrity. A bright-field image (Fig. 1c) shows a dense, defect-free coating along the growth direction. HRTEM (Fig. 1d) clearly resolves the intrinsic nanolayered architecture of Ti_3AlC_2. Area I display periodic stacking of triple Ti(C) layers and single Al layers, with a measured *c*-lattice parameter of 1.857 nm, consistent with reported values [34]. The fast Fourier transform pattern (FFT) from Area II corresponds to a lattice spacing of d = 0.223 nm, matching the theoretical (104) interplanar distance of Ti_3AlC_2. HAADF-STEM elemental mapping (Fig. 1e) demonstrates homogeneous spatial distribution of Ti, Al, and C, confirming overall chemical uniformity. Collectively, a high-purity Ti_3AlC_2 MAX phase coating with high crystallinity, uniform composition, and intact nano-layered structure has been successfully fabricated.

3.2. Electrochemical corrosion behaviors

The OCP serves as a key indicator of surface state and passive behavior, with its evolution over immersion time directly revealing physical and chemical changes at the material-solution interface and offering insights into the thermodynamic characteristics and extent of corrosion damage in a given medium [35]. Fig. 2 presents OCP-time curves for the Ti_3AlC_2 coating and Ti-6Al-4V substrate in 3.5 wt.% NaCl solution. At the onset of testing, the OCP of the Ti_3AlC_2 coating was −0.24 V, markedly nobler than that of the Ti-6Al-4V substrate (−0.63 V), indicating a lower thermodynamic tendency for corrosion. Over time, the OCP shifted rapidly toward more positive values before stabilizing, reflecting the self-passive behavior typical of passive materials [36]. This trend can be quantitatively described by a biexponential decay function:

$$E_{OCP} = a \times e^{-t/t_1} + b \times e^{-t/t_2} + c \tag{2}$$

where *a*, *b*, and *c* are constants, while t_1 and t_2 represent the time constants associated with the initial nucleation and subsequent thickening of the passive film, respectively. Fitting results (Fig. 2) show that t_1 is substantially smaller than t_2, indicating rapid surface oxidation and

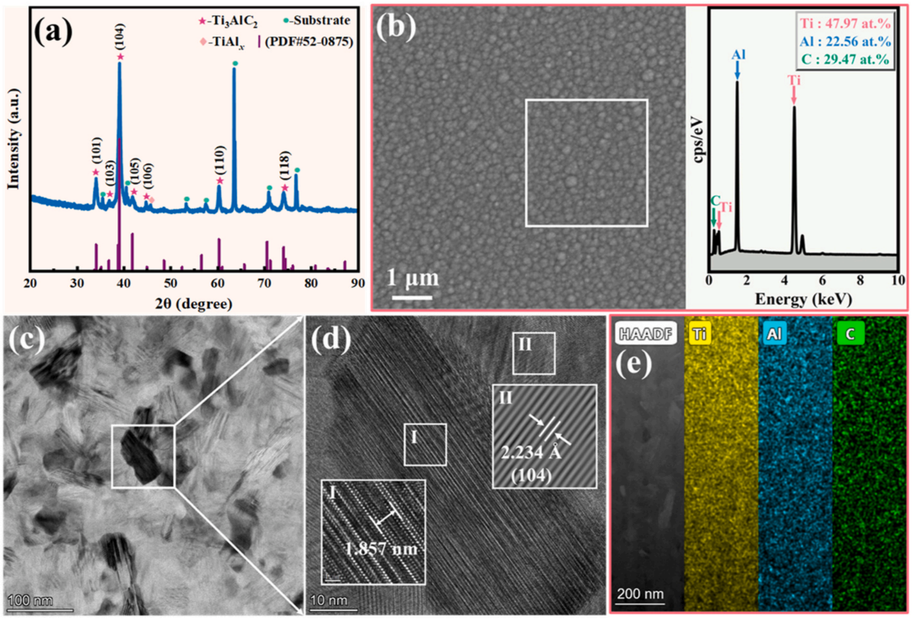

Fig. 1. Microstructure of Ti_3AlC_2 coating. (a) XRD pattern of the prepared coating, (b) Surface morphology of the coating and the corresponding EDS results, (c)-(d) TEM and HRTEM images, (e) EDS element mapping of Ti, Al and C.

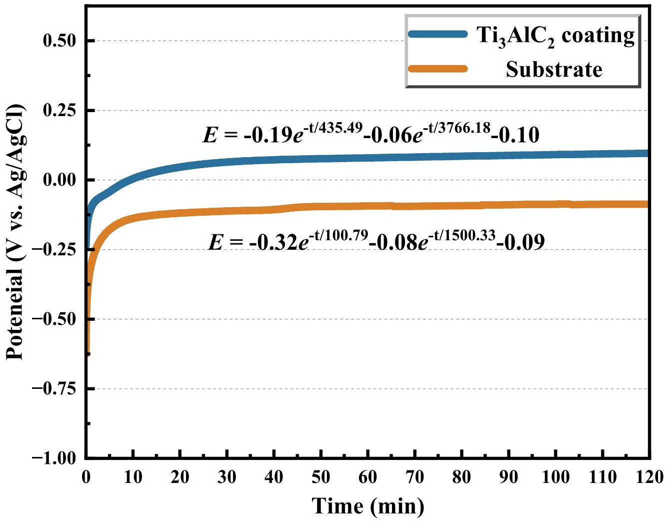

Fig. 2. E_{OCP}-time plots for Ti$_3$AlC$_2$ coating and substrate in 3.5 wt.% NaCl solution.

initial passive film formation upon exposure to the corrosive medium, effectively suppressing anodic dissolution. Thereafter, a period of slower film thickening and structural reorganization proceeds until the rates of film formation and dissolution equilibrate. Under steady-state, the OCP of the Ti$_3$AlC$_2$ coating stabilized at 0.09 V, still markedly higher than that of the Ti-6Al-4V substrate (−0.08 V). Moreover, the smoother and more stable OCP profile of the coating suggests superior thermodynamic stability and structural compactness of its passive film. Overall, the Ti$_3$AlC$_2$ MAX phase coating, owing to its favorable chemical stability and self-passivating capability, forms a dense and stable passive layer that effectively barriers corrosive species and significantly enhances the corrosion resistance of the underlying substrate.

EIS was performed at the open circuit potential after 2 h of immersion in 3.5 wt% NaCl solution.

The Nyquist plots (Fig. 3a) exhibit a single capacitive loop, though none form a complete semicircle, indicating non-ideal capacitive behavior at the coating/solution interface. A larger capacitive loop radius generally corresponds to higher charge transfer resistance and superior corrosion resistance [37,38]. The Ti$_3$AlC$_2$ coating displays a significantly larger loop than the Ti-6Al-4V substrate, consistent with its enhanced corrosion resistance. The improvement stems from the layered structure of Ti$_3$AlC$_2$, which facilitates the formation of a dense and stable passive film that effectively hinders the adsorption and penetration of corrosive medium. Bode plots (Fig. 3b) further elucidate the dynamic polarization behavior. In the high-frequency range (10^5-10^3 Hz), a flat plateau around $|Z| \approx 10$ Ω•cm^2 corresponds to the solution resistance, confirming a well-controlled ohmic drop in the experimental setup. The phase angle approaches 0° around 10^4-10^5 Hz, indicating dominant electronic conduction. Within the mid-frequency region (10^2–10^{-1} Hz), the slope of $lg|Z|$ versus $lg\,f$ nears −1 while the phase angle remains around 80°, reflecting the relaxation process of the passive film capacitance. The broader high-phase-angle plateau of the Ti$_3$AlC$_2$ coating, compared to that of the substrate, suggests a more complete passive film with stable dielectric properties. The low-frequency impedance modulus directly reflects long-term corrosion resistance. At 0.01 Hz, the Ti$_3$AlC$_2$ coating exhibits an impedance value one order of magnitude higher than the substrate, demonstrating the superior barrier capability of its passive film against corrosive medium penetration and reaction suppression.

The EIS data were fitted using an equivalent electrical circuit (inset of Fig. 3a) to quantitatively describe the electrochemical characteristics of the surface/interface and to reveal the underlying correlation between the microstructure of Ti$_3$AlC$_2$ and its corrosion resistance. The model $R_s(Q_c(R_p(Q_{dl}R_{ct})))$ was adopted to represent the passive film structure [39,40]. The equivalent circuit model comprises the solution resistance (R_s), passive film resistance (R_p), charge transfer resistance (R_{ct}), and constant phase elements (CPE), with the latter employed to account for the deviation from ideal capacitive behavior. Specifically, Q_c and Q_{dl} represent the capacitive behavior of the passive film and the double layer, respectively. Additionally, n_c and n_{dl} denote the exponential indices of the constant phase elements CPE$_c$ and CPE$_{dl}$, where the value of n reflects the extent to which the passive film characteristics deviate from those of a pure capacitor (n = 1 corresponds to ideal capacitive behavior) [41]. A higher R_p value typically indicates a denser passive film providing better protection [42]. Similarly, a larger R_{ct} reflects greater inhibition of charge transfer reactions during corrosion [43]. Because the measured capacitive response never reached the theoretical −90° maximum phase angle of an ideal dielectric, a CPE was used instead of a pure capacitor (C) [44]. The impedance of a CPE is defined as:

$$Z_{CPE} = \left[Y(j2tf)^n\right]^{-1} \tag{3}$$

Here, j is the imaginary unit, f is frequency, Y is a proportionality factor, and n is an exponent. A value of n = 1 corresponds to ideal capacitive behavior, indicating a homogeneous surface, whereas a deviation from unity reflects distributed charge transfer processes and surface roughness induced dispersion. As shown in Fig. 3, the fitted curves exhibit excellent agreement with the experimental data, with all

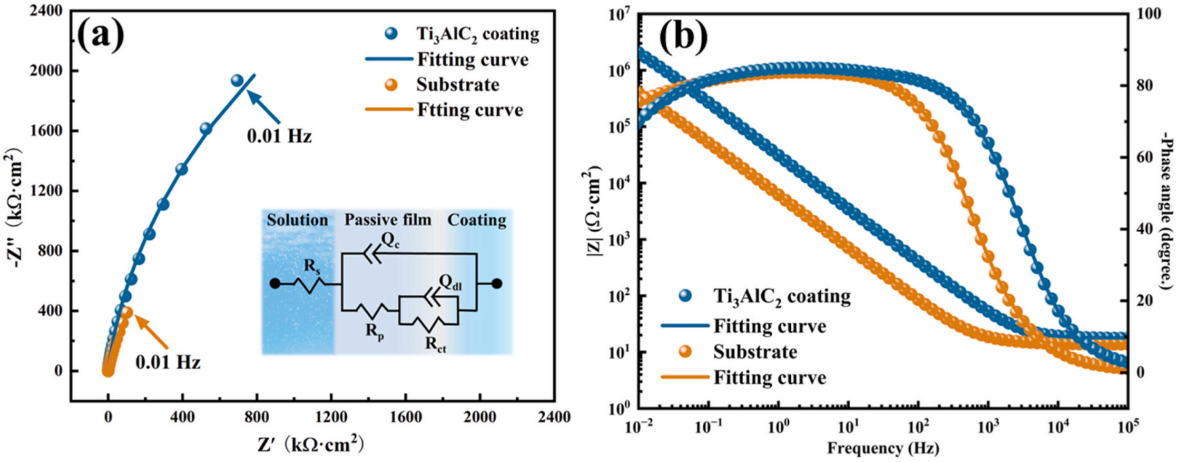

Fig. 3. (a) Nyquist plots and equivalent electrical circuit (EEC) used to fit the impedance spectra, (b) Bode plots of the Ti$_3$AlC$_2$ coating and Substrate after 2 h of immersion at respective OCPs in the 3.5 wt.% NaCl solution.

chi-squared values (χ^2) on the order of 10^{-4}, confirming that the selected equivalent circuit accurately represents the electrochemical behavior of the samples in 3.5 wt.% NaCl solution. The fitted electrochemical parameters are summarized in Table 1. The R_p for the Ti_3AlC_2 coating is on the order of $\sim 10^2$ Ω cm^2, significantly higher than that of the substrate. This indicates the formation of a protective passive layer that effectively hinders further penetration of corrosive species. Moreover, the R_{ct} reaches 8.01×10^6 Ω•cm^2, demonstrating strong suppression of interfacial electrochemical reactions. Together, these results clearly reflect the superior corrosion resistance of the Ti_3AlC_2 coating.

Fig. 4 presents the potentiodynamic polarization curves of the Ti_3AlC_2 coating and the Ti-6Al-4V substrate, along with the derived electrochemical parameters obtained via Tafel extrapolation. As shown in Fig. 4a, the cathodic current gradually decreases with increasing potential, followed by a spontaneous passive region in the anodic branch for all samples. The corrosion potential (E_{corr}) reflects the thermodynamic tendency for corrosion, while the corrosion current density (i_{corr}) describes the kinetic rate of the process [45]. Compared with the substrate, the anodic branch of the Ti_3AlC_2 coating shifts toward nobler potentials and significantly lower current densities. The coating exhibits an i_{corr} of 4.43×10^{-10} A•cm^{-2}, approximately two orders of magnitude lower than that of the substrate, alongside a more positive E_{corr} (Fig. 4b). These results demonstrate the markedly enhanced electrochemical inertness and corrosion resistance imparted by the Ti_3AlC_2 coating in NaCl solution.

3.3. *Passive film investigations*

3.3.1. *Steady-state passive film properties*

To investigate the passive film formation process, potentiostatic polarization was performed on the Ti_3AlC_2 coating at potentials of 0.5 V, 0.8 V, and 1.0 V relative to the stable open circuit potential for 10 h. As shown in Fig. 5a, the current density at all applied potentials decreased rapidly during the initial stage (0~30 min). This decline is attributed to the fast surface oxidation and formation of a passive film under constant potential, which strongly suppresses the anodic dissolution and leads to a sharp drop in the corrosion rate, reflected by the current density. After approximately 1 h, the current density gradually stabilized, though local fluctuations persisted, indicating concurrent local dissolution and reform during film growth. In the steady state region (6~10 h, see inset), the lowest current density was observed at 0.8 V, suggesting optimal corrosion resistance under this potential. Fig. 5b displays the logarithmic current density (*lgi*) versus logarithmic time (*lgt*). During the initial film growth stage, the *lgi*-*lgt* curves exhibited a linear descending trend at all potentials, consistent with the kinetics described by the high-field model for passive film growth [46]. This indicates that the film formation rate substantially exceeded its dissolution rate in this period. According to the Macdonald model [47,48], the relationship between current density and time can be expressed as:

$$lgi = A - nlgt \tag{4}$$

where i is the current density, A is a constant, n is the passive exponent, and t is time. The passive exponent n indirectly reflects the compactness and protective quality of the passive film. A value of n close to 1 suggests a dense, highly protective film, whereas $n \approx 0.5$ implies a porous structure. Fitting the linear regions in Fig. 5b yielded similar passive exponents of 0.75, 0.71, and 0.77 for 0.5 V, 0.8 V, and 1.0 V, respectively, indicating that the films formed under different potentials all provide effective corrosion protection.

Fig. 5c and d presents the EIS of the Ti_3AlC_2 coating after 10 h of potentiostatic polarization at different potentials. The Nyquist plots (Fig. 5c) display a single capacitive loop under all conditions, with similar spectral shapes. The diameter of the capacitive loops increases in the order 0.5 V < 1.0 V < 0.8 V, indicating that the passive film formed at 0.8 V possesses the highest interfacial impedance and optimal corrosion resistance. The Bode plots (Fig. 5d) provide further insight into the frequency-dependent behavior. The impedance modulus (|Z|) plateau in the high-frequency region (>10^3 Hz), corresponding to the solution resistance, shows little variation with potential, confirming a consistent ohmic drop in the system. In the mid-frequency range (10^3-10^{-1} Hz), the phase-angle peaks remain near 80°. The films formed at 0.8 V and 1.0 V sustain this high phase angle over a broader frequency range, reflecting capacitive behavior closer to the ideal state. The low-frequency (0.01 Hz) impedance modulus is substantially higher for the films formed at 0.8 V and 1.0 V compared to that at 0.5 V. The EIS data were fitted using the equivalent circuit model $R_s(Q_c(R_p(Q_{dl}R_{ct})))$ introduced earlier. The fitted curves show excellent agreement with the experimental data (Fig. 5c and d), supported by chi-squared values (χ^2) on the order of 10^{-4}, which validates the model applicability and data reliability. The detailed fitting parameters are summarized in Table 2. The fitted results reveal that the R_{ct} remains high following potentiostatic polarization, with R_{ct} consistently exceeding the R_p across all conditions, indicating that corrosion inhibition is predominantly governed by the charge transfer process. The lower R_p observed at 0.5 V suggests a less compact passive film. In contrast, the films induced at 0.8 V and 1.0 V are denser and more stable, demonstrating superior protective performance.

3.3.2. *Chemical composition of formed passive film*

To elucidate the chemical composition and atomic bonding states of the passivation film formed on the Ti_3AlC_2 coating after potentiostatic polarization at 0.5 V, high-resolution XPS characterization was conducted. Fig. 6a–d presents the high-resolution XPS spectra of Ti 2p, Al 2p, C 1s, and O 1s for the as-received (non-etched) surface. The Ti 2p spectrum (Fig. 6a) exhibited relatively weak titanium signals, with peaks at 455.9 and 462.0 eV assigned to Ti $2p_{1/2}$ and Ti $2p_{3/2}$ of Ti-C bonds in titanium carbide compounds [49], respectively. The presence of these features is associated with Al outward diffusion during passivation. The Al 2p spectrum (Fig. 6b) displayed a single peak at a binding energy of 75.4 eV, corresponding to Al-O bonds [37]. Deconvolution of the high-resolution C 1s spectrum (Fig. 6c) revealed four distinct components, peaks at approximately 284.8, 286.0, and 288.5 eV were attributed to sp^2 and sp^3 hybridized carbon species formed during oxidation and surface-adsorbed organic contaminants containing C=O groups [50], while the peak at 280.8 eV was assigned to C-Ti bonds [49]. The O 1s spectrum (Fig. 6d) showed a single peak at 532.3 eV, characteristic of O-Al bonding [51]. After Ar^+ ion etching, the Ti 2p spectrum (Fig. 6e) exhibited not only Ti-C bonding features but also an additional peak at 454.8 eV, attributed to the underlying Ti_3AlC_2 [52]. Deconvolution of the Al 2p spectrum (Fig. 6f) revealed an extra low-intensity peak at 73.8 eV compared to the non-etched sample, ascribed to Al-Ti bonding associated with the Ti_3AlC_2 phase [53]. In the C 1s spectrum (Fig. 6g), besides the sp^2 hybridized carbon peak at 284.8 eV, a distinct C-Ti peak was identified at 281.7 eV [49]. This C-Ti peak originates from

Table 1

EEC parameters for the EIS data of the Ti_3AlC_2 coating and substrate at their respective OCPs.

Sample	R_s (Ω cm^2)	CPE$_c$		R_p (Ω cm^2)	CPE$_{dl}$		R_{ct} (Ω cm^2)	χ^2 (10^{-4})
		Q_c (Ω^{-1} cm^{-2} s^n)	n_c		Q_{dl} (Ω^{-1} cm^{-2} s^n)	n_{dl}		
Ti_3AlC_2 coating	17.80 ± 0.08	$4.33 \pm 0.31 \times 10^{-6}$	0.960 ± 0.006	$2.17 \pm 0.71 \times 10^2$	$1.48 \pm 0.31 \times 10^{-6}$	0.857 ± 0.007	$8.01 \pm 0.38 \times 10^6$	2.72
Substrate	13.95 ± 0.04	$1.14 \pm 0.03 \times 10^{-5}$	0.998 ± 0.009	13.65 ± 1.79	$1.85 \pm 0.03 \times 10^{-5}$	0.872 ± 0.002	$3.05 \pm 0.16 \times 10^5$	1.18

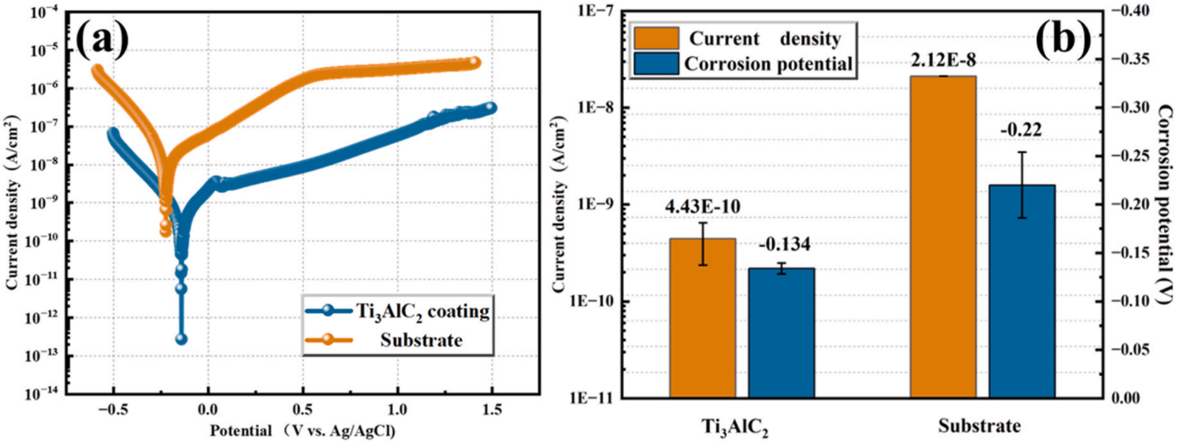

Fig. 4. (a) Potentiodynamic polarization curves of Ti_3AlC_2 coating and Substrate in 3.5 .wt% NaCl solution. (b) Corrosion current densities and corrosion potentials.

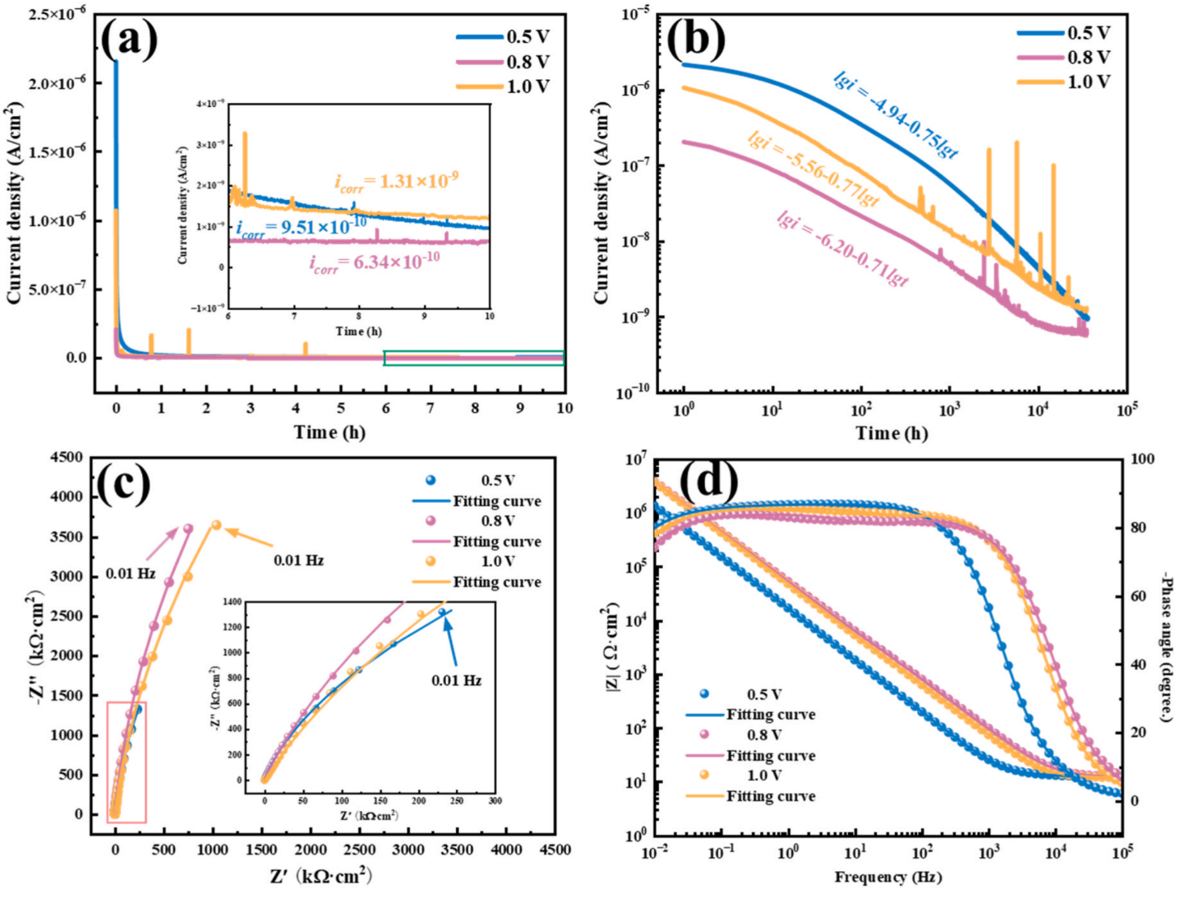

Fig. 5. (a) The current density versus time curves, (b) The log$i$-log$t$ curves, (c) Nyquist plots and (d) Bode plots of Ti_3AlC_2 coating after potentiostatic polarization at 0.5V, 0.8V and 1.0V (vs. the stable OCP) for 10 h in 3.5 wt.% NaCl solution.

Table 2

EEC parameters for the EIS data of the Ti_3AlC_2 coating after potentiostatic polarization at 0.5V, 0.8V and 1.0V (vs. the stable OCP) for 10 h in 3.5 wt% NaCl solution.

Coating		R_s (Ω cm²)	CPE_c		R_p (Ω cm²)	CPE_{dl}		$R_{ct} \times 10^7$ (Ω cm²)	χ^2 (10^{-4})
			Q_c (Ω^{-1} cm^{-2} s^n)	n_c		Q_{dl} (Ω^{-1} cm^{-2} s^n)	n_{dl}		
Ti_3AlC_2	0.5 V	12.11 ± 0.02	$5.90 \pm 0.12 \times 10^{-6}$	0.992 ± 0.001	11.22 ± 1.40	$4.42 \pm 0.13 \times 10^{-6}$	0.92 ± 0.01	1.19 ± 0.04	0.27
	0.8 V	11.52 ± 0.02	$3.49 \pm 0.03 \times 10^{-6}$	0.949 ± 0.001	$2.70 \pm 0.53 \times 10^4$	$1.77 \pm 0.33 \times 10^{-7}$	0.98 ± 0.02	2.71 ± 0.08	0.38
	1.0 V	11.88 ± 0.04	$3.13 \pm 0.04 \times 10^{-6}$	0.931 ± 0.002	$3.57 \pm 0.68 \times 10^4$	$3.08 \pm 0.45 \times 10^{-7}$	0.96 ± 0.02	2.33 ± 0.11	1.49

both the Ti_3AlC_2 MAX phase and the Ti_3C_2 formed after Al deintercalation from the Ti_3AlC_2 structure. The O 1s spectrum (Fig. 6h)

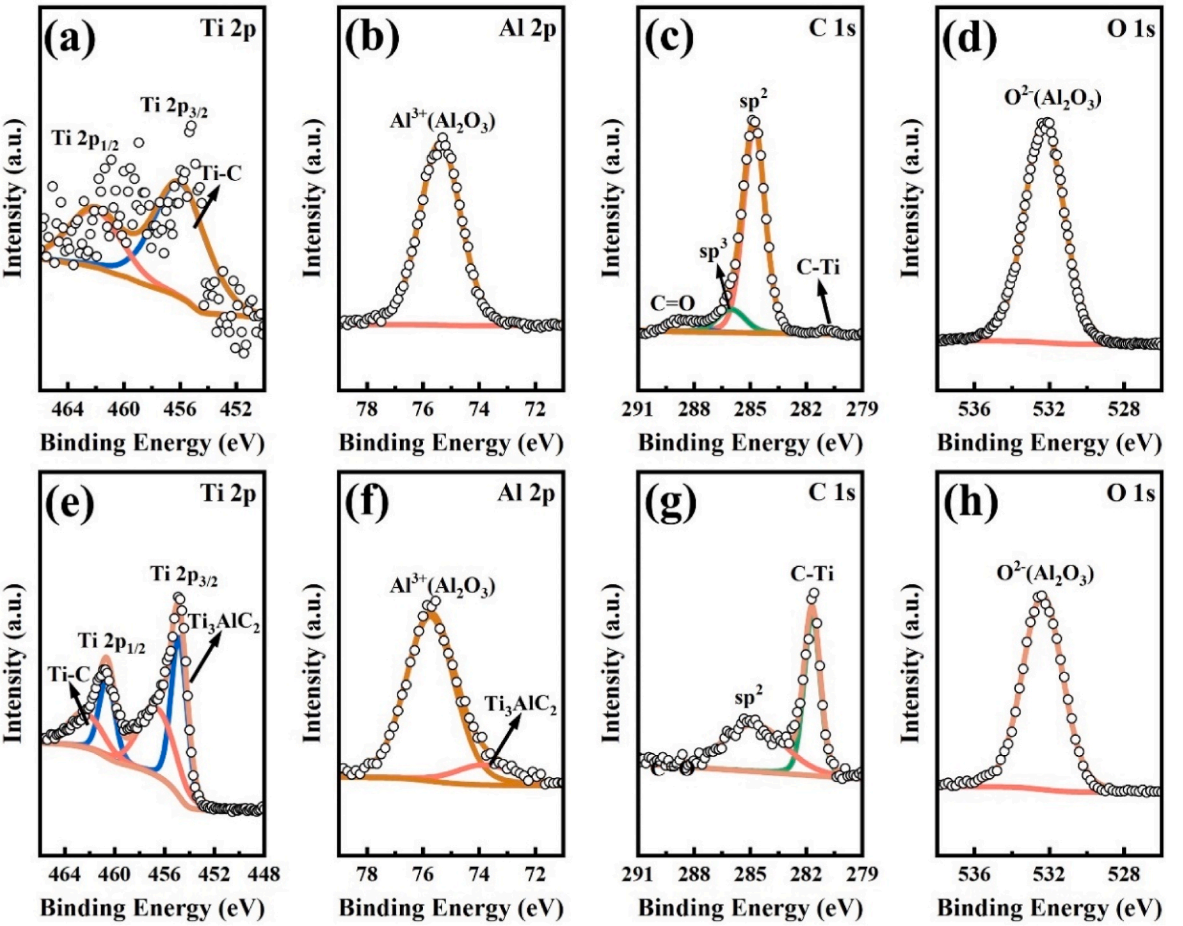

Fig. 6. High resolution XPS spectra of the passive film formed on the Ti_3AlC_2 coating after potentiostatic polarization at 0.5 V (vs. the stable OCP) for 10 h: (a)-(d) and (e)-(f) correspond to the Ti 2p, Al 2p, C 1p and O 1s before and after ions sputtering for 3min, respectively.

remained essentially unchanged after etching. Collectively, the XPS results indicate that the passivation film formed on the Ti_3AlC_2 coating surface is predominantly composed of Al_2O_3.

3.3.3. Mott-Schottky analysis

Mott-Schottky (M−S) analysis elucidates the semiconductor properties of passive films formed on metal surfaces. Upon application of an external voltage to the electrode, the potential drop occurs primarily across the space charge region of the oxide film, modulating its capacitance (C_{SC}) with applied potential (E). According to M − S theory, the interfacial capacitance can be described by the following equations [54]:

$$\frac{1}{C_{CS}^2} = \frac{2}{\varepsilon\varepsilon_0 e N_D}\left(E - E_{fb} - \frac{e}{kT}\right) \tag{5}$$

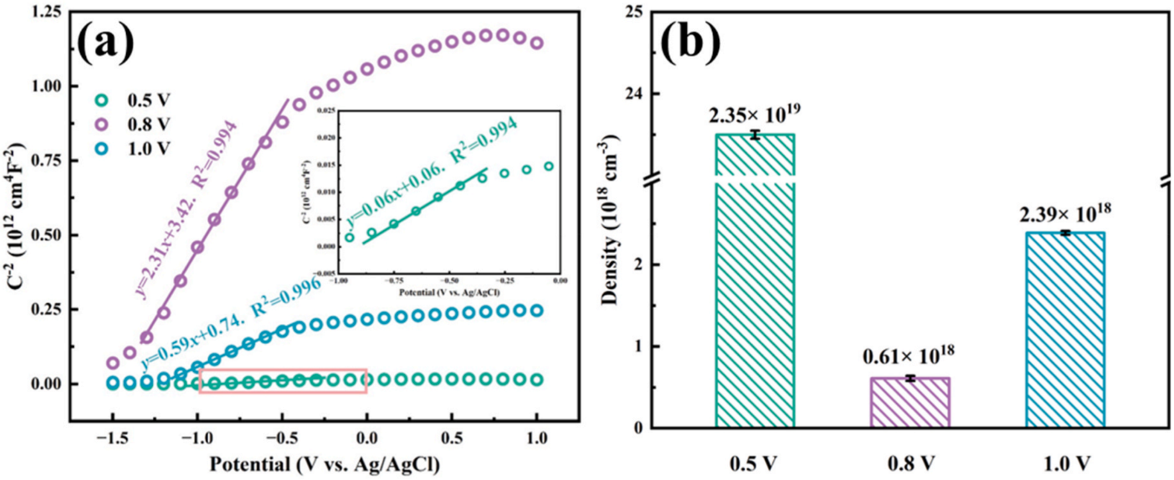

Fig. 7. (a) Mott-Schottky plots and (b) the corresponding donor densities of the passive films formed on the Ti_3AlC_2 coating after 10 h of potentiostatic polarization at various potentials in 3.5 .wt% NaCl solution.

$$N_D = \frac{2}{\varepsilon\varepsilon_0 e}\left[\frac{d(C_{CS}^{-2})}{dE}\right]^{-1} \tag{6}$$

where ε_0 is the vacuum permittivity (8.85×10^{-14} F•cm^{-1}), e is the elementary charge (1.602×10^{-19} C), N_D is the donor density (for an n-type semiconductor), E_{fb} is the flat-band potential, k is the Boltzmann constant (1.38×10^{-23} J•K^{-1}), T is temperature, and ε is the dielectric constant of the passive film. Based on the subsequent microstructural characterization confirming the film as single Al_2O_3, a value of $\varepsilon = 10$ was used [55]. Fig. 7a presents M−S plots for the passive films formed on the Ti_3AlC_2 coating after 10 h at different polarization potentials in 3.5 wt.% NaCl solution. All curves exhibit a positive slope, with C_{CS}^{-2} increasing linearly as the potential shifts anodically, indicating n-type semiconductor behavior of the passive film [56]. This characteristic is consistent with reported semiconductor properties of Al_2O_3 film, where oxygen vacancies or interstitial cations act as the dominant charge carriers. Notably, the slope varies with polarization potential, increasing initially and then decreasing. A lower donor density generally correlates with fewer defects, improved structural integrity, and enhanced corrosion resistance [57]. Using Eq. (6), the donor density N_D was calculated from the linear region of each M−S plot. As summarized in Fig. 7b. N_D is relatively high for films formed at 0.5 V, suggesting a defective structure. When the polarization potential increases to 0.8 V, N_D reaches its minimum value among the three conditions, indicating the formation of a more compact and less defective passive film. However, a further increase to 1.0 V leads to a resurgence in N_D. In summary, the passive film formed on Ti_3AlC_2 coatings under anodic polarization at 0.8 V exhibits the highest structural compactness and thus provides the most effective corrosion protection for the underlying material.

3.3.4. Passive film growth behavior

As shown in Fig. 5a, the potentiodynamic polarization curve of the Ti_3AlC_2 coating at 0.5 V (vs. stable OCP) exhibits the highest stability with the lowest susceptibility to pitting corrosion. To investigate the growth behavior of the Ti_3AlC_2 coating during electrochemical corrosion, a successive electrochemical impedance spectroscopy (SEIS) test was performed under potentiostatic polarization at 0.5 V (vs. stable OCP) for 10 h, with impedance spectra recorded every 30 min. [58]. In the Nyquist plot (Fig. 8a), each curve corresponds to the interfacial impedance at a specific time, and the radius of the capacitive arc directly reflects the total interfacial impedance. Initially, the small loop radius indicates the absence of a protective passive film on the coating surface, resulting in low corrosion resistance. With prolonged polarization, the gradual increase in loop radius suggests the formation and growth of a passive film with improved protective properties, leading to a significant increase in total impedance and enhanced resistance against corrosive medium penetration and interfacial reactions. In the Bode plot (Fig. 8b), the impedance modulus |Z| at the low-frequency region (0.01 Hz) increases over time, confirming the development of a highly resistive and barrier-like passive film that effectively impedes long-term chloride ion penetration and attack. The phase angle curve (Fig. 8c) exhibits a high peak value (80°). As potentiostatic polarization proceeds, the high phase angle peak is maintained in the mid-frequency range, and the frequency range covered by the peak broadens, reflecting improved homogeneity and densification of the passive film along with a reduction in defect density.

Furthermore, the capacitance (C_P) of the passive film can be estimated using the Hsu-Mansfeld formula [59] based on parameters Q_c and n_c obtained from CPE fitting. The thickness of the passive film δ can then be approximated from this effective capacitance value C_P [60]. The expression is as follows:

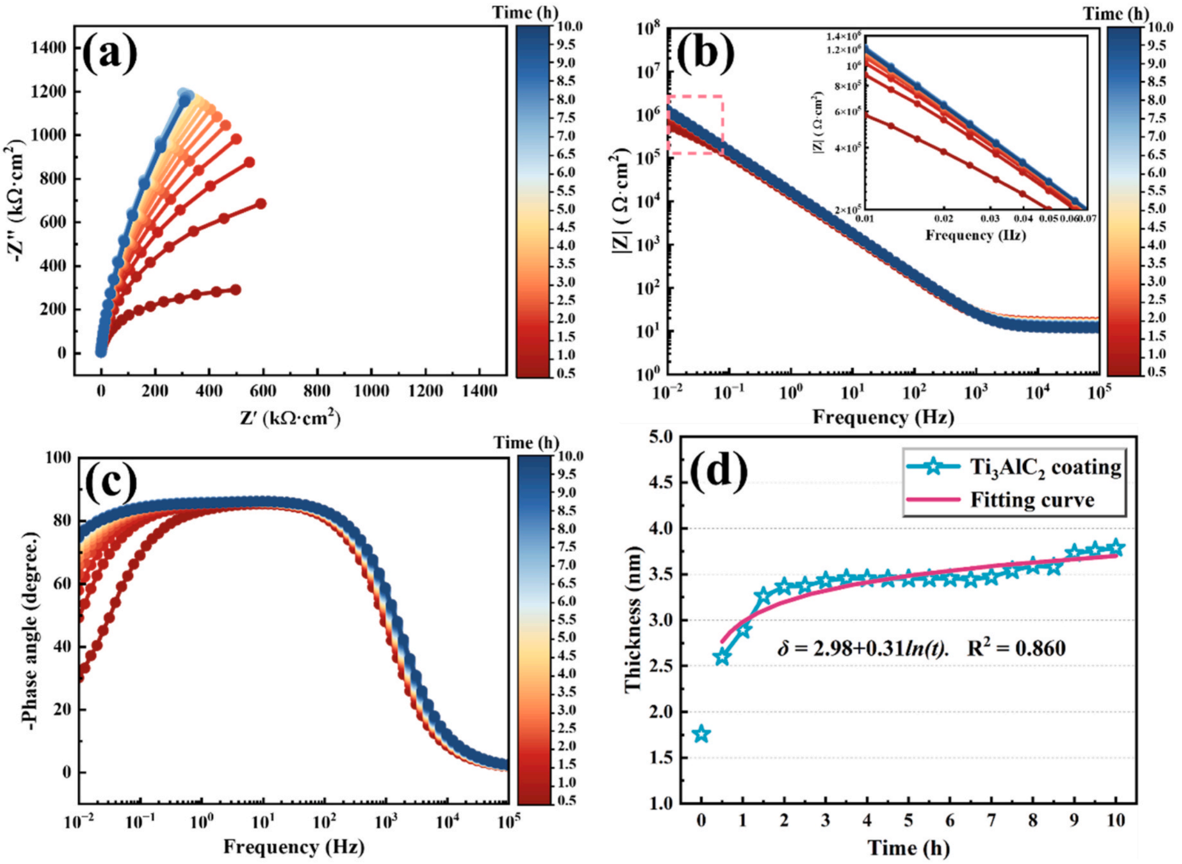

Fig. 8. Evolution of EIS spectra and physical parameters versus time of the passive film form on the Ti_3AlC_2 coating in 3.5 wt.% NaCl solution. (a) Nyquist plots, (b)-(c) Bode plots and (d) The passive film thickness.

$$C_P = Q_C^{\frac{1}{n}}(R_P)^{\frac{1-n}{n}} \tag{7}$$

$$\delta = \frac{\varepsilon_0 \varepsilon A}{C_P} \tag{8}$$

where ε_0 is the vacuum permittivity, ε is the dielectric constant of the passive film (taken as 10), and A is the exposed electrode area (0.2 cm^2). The calculated passive film thickness is shown in Fig. 8d. At open circuit potential, the passive film formed on the Ti_3AlC_2 coating under natural corrosion conditions is approximately 1.76 nm (film thickness at $t = 0$ in Fig. 8d). Under an applied anodic potential of 0.5 V, the film thickness evolution over time ($t > 0$) exhibits an initial rapid growth followed by stabilization. In the early stage ($t < 2$ h), the anodic potential drives vigorous oxidation, promoting rapid combination of metal cations and oxygen anions to form an oxide layer, leading to a high growth rate and a rapid increase in thickness to about 3.37 nm. As time proceeds, the film growth rate gradually balances with the dissolution rate caused by the corrosive medium. After 6 h of polarization, a slight further increase in film thickness is observed, attributed to selective oxidation at defect sites, where newly formed oxides fill defects and extend the film surface, resulting in a modest overall thickness increase. The growth behavior of the passive film thickness δ over time t under anodic polarization can be fitted by the expression as follows [61].

$$\delta = A + B\ln(t) \tag{9}$$

where A and B are constants. As shown in Fig. 8d, the fitting result indicates that the passive film growth on the Ti_3AlC_2 coating follows a logarithmic law, suggesting that the film growth during electrochemical corrosion is controlled by ion transport processes. According to the high-field migration and point defect diffusion model [61,62], during the early stage of electrochemical passive, the passive film is thin and the electric field across it is strong. This high field acts as a driving force that significantly accelerates the transport of metal cations or oxygen anions across the film, promoting rapid film growth. As the film thickens, the electric field strength decreases inversely with thickness, slowing down ion migration and consequently reducing the film growth rate. Moreover, the growth of the passive film relies on the diffusion of point defects such as oxygen vacancies and metal interstitials. With increasing film thickness, the transport path for these defects lengthens, reducing their effective accumulation rate and further decelerating film growth.

To elucidate the microstructure of the passive film, TEM characterization further revealed the microstructure of the passive film. As shown in Fig. 9a, a uniform, continuous, and dense passive film formed on the coating surface. HAADF imaging and corresponding elemental maps (Fig. 9b) demonstrated strong Al and O signals within the film region, with Ti signals being markedly absent, again confirming the aluminum oxide dominated composition. EDS point analysis (Fig. 9e) of Area I in Fig. 9a yielded atomic percentages of 32.36 at.% Al and 62.51 at.% O, corresponding to an Al/O ratio close to 1:1.5, consistent with the stoichiometry of Al_2O_3 and supporting the XPS conclusions. Beneath the passive film, an oxygen-diffusion zone (Area II) was observed. This transition region contained Ti, Al, and O, but elemental mapping indicated that the inward-diffused oxygen primarily co-localized with Al, resulting in a zone enriches Al and O but Ti-depleted. This suggests preferential reaction of oxygen with Al during inward diffusion. EDS analysis of Area III confirmed a Ti/Al/C atomic ratio of approximately 3:1:2, matching the standard stoichiometry of the Ti_3AlC_2 and indicating preservation of the MAX phase crystal structure. HRTEM imaging (Fig. 9c) of the area marked by the white square in Fig. 9a showed no distinct lattice fringes within the passive film or the diffusion zone, indicating a predominantly amorphous structure. The measured passive film thickness was approximately 4.07 nm, aligning well with the thickness estimated from SEIS data. FFT analysis of the diffusion zone shows a diffraction pattern dominated by amorphous or nanocrystalline structures (Fig. 9d). Overall, the passive film formed on the Ti_3AlC_2 coating is composed primarily of amorphous Al_2O_3. Below this film lies an oxygen-diffusion transition zone dominated by aluminum oxide, while the underlying MAX phase matrix retains its crystalline structure.

3.3.5. Formation mechanism of passive film

MAX phase materials possess a distinctive layered crystal structure in which the A-layer elements are bonded relatively weakly to adjacent M_6X layers. This configuration enables the selective de-intercalation of A-site elements under external energy input [26]. The formation of electrochemical corrosion-induced passivation films occurs at the interface between the coating and the electrolyte, with film composition primarily governed by the relative diffusion kinetics of constituent elements within the coating. Vacancy formation energy, which quantifies the energy required for an atom to detach from its lattice site, directly

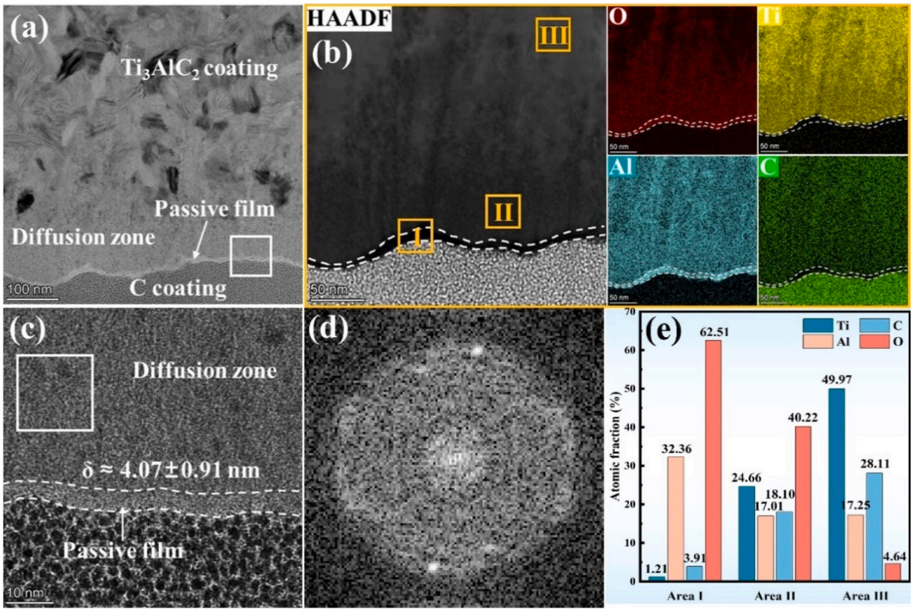

Fig. 9. TEM images of the passive film after SEIS test. (a) TEM bright image, (b) STEM-HAADF image and elemental maps, (c) HRTEM image at the interface between the passive film and Ti_3AlC_2 coating, (d) corresponding SAED pattern, (e) Elemental fraction of area I, II and III.

determines the propensity for defect generation and atomic migration. As illustrated in Fig. 10, the crystal structure of Ti_3AlC_2 contains two distinct types of Ti atoms. In this work, the Ti_I atomic layers are adjacent to Al atomic layers, whereas the Ti_{II} atomic layers form sandwich-like configurations with double C atomic layers. DFT calculations reveal vacancy formation energies of 5.67 eV and 7.48 eV for Ti_I and Ti_{II} atoms, respectively, in contrast to a significantly lower value of 2.77 eV for Al atoms. This nearly three-fold energy difference indicates that Al vacancies form most readily in Ti_3AlC_2. During electrochemical corrosion, the low Al vacancy formation energy substantially reduces the energy barrier for Al atom detachment from the M-A interlayers, enabling their rapid outward migration along lattice defects to the material surface where they accumulate. Moreover, the Al vacancy formation energy in Ti_3AlC_2 exhibits a negative correlation with vacancy concentration, which decreases as the number of pre-existing vacancies increases [63]. This behavior indicates that existing Al vacancies facilitate the formation of additional vacancies, thereby exerting a positive feedback effect that further enhances the outward diffusion kinetics of Al atoms. Conversely, the high Ti vacancy formation energies severely suppress the bulk diffusion of Ti atoms, thereby hindering their participation in surface oxidation reactions. Consequently, during the initial passivation stage, the preferentially enriched surface Al atoms react selectively with environmental oxygen to form a continuous and dense Al_2O_3 passivation film (Eqs. 10 and 11). Furthermore, Al_2O_3 possesses a considerably more negative ΔG (−1582.3 kJ/mol) compared to TiO_2 (−889.4 kJ/mol) at ambient temperature [64,65]. Since a more negative ΔG signifies greater thermodynamic stability and a stronger tendency for formation, this difference further reinforces the thermodynamic driving force favoring selective Al oxidation.

$$O_2 + 2H_2O + 4e^- \rightarrow 4OH^- \tag{10}$$

$$2Al + 6OH^- \rightarrow Al_2O_3 + 3H_2O + 6e^- \tag{11}$$

The growth of the passive film follows a high-field model, where the growth rate is limited by ion migration through the existing oxide layer. For Al_2O_3, growth relies on both inward migration of oxygen anions (O^{2-}) and outward migration of aluminum cations (Al^{3+}), with the former contributing dominantly (approximately 90%) [66]. Once a continuous Al_2O_3 film forms, O^{2-} must migrate inward through this layer to reach the reaction interface, while the low mobility of Al^{3+} leads to an exponential decay in growth rate over time, eventually reaching a dynamic steady state. Notably, Li et al. reported that a Ti_2AlC coating also forms a single Al_2O_3 passive film after electrochemical corrosion, but without a discernible oxygen-diffusion zone beneath it [18]. This contrasts with the results observed for Ti_3AlC_2 in this study, a difference primarily arising from the distinct kinetic behaviors dictated by their respective Al contents. The atomic percentage of Al in Ti_3AlC_2 is approximately 16.7%, lower than the 25% in Ti_2AlC. In Ti_3AlC_2, after the depletion of surface Al, internal Al must diffuse over a longer distance to reach the interface. Simultaneously, oxygen penetrates inward through vacancies or pores left by the de-intercalated Al. The two species meet and react internally, resulting in the formation of an Al and O-enriched diffusion transition zone. This zone structurally bridges the passive film and the coating bulk, preventing film delamination caused by structural destabilization due to Al loss and thereby enhancing the continuity and protective performance of the passive film. In summary, the formation of a single Al_2O_3 passive film accompanied by an oxygen-diffusion zone on Ti_3AlC_2 during electrochemical corrosion results from the combined effects of thermodynamically favored oxidation and kinetically controlled diffusion. The Al_2O_3 film originates from the strong thermodynamic driving force for Al oxidation and high-field growth kinetics. The emergence of the oxygen-diffusion zone is closely associated with the lower Al content in Ti_3AlC_2, which promotes inward oxygen penetration and subsurface oxidation. A schematic illustrating the corrosion passive process of the Ti_3AlC_2 coating in 3.5 .wt% NaCl solution is presented in Fig. 11.

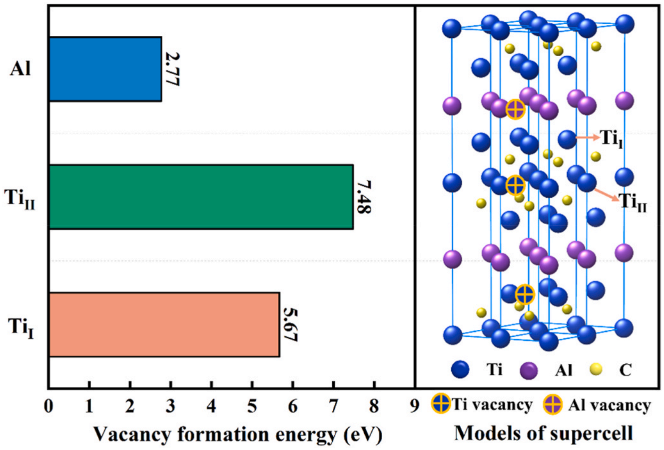

Fig. 10. Vacancy formation energies of Ti/Al atoms and models of supercell in Ti_3AlC_2 coating.

4. Conclusions

In this study, a Ti_3AlC_2 MAX phase coating was successfully synthesized on a Ti-6Al-4V alloy substrate via HiPIMS followed by post-deposition annealing. Systematic electrochemical testing and microstructural characterization were employed to investigate the electrochemical behavior of coating and the formation mechanism of its surface passive film in a neutral 3.5 wt.% NaCl solution. The Ti_3AlC_2 coating exhibited superior corrosion resistance, demonstrating a corrosion current density of 5.74×10^{-10} A•cm^{-2}, approximately two orders of magnitude lower than that of the Ti-6Al-4V substrate. Electrochemical impedance spectroscopy further confirmed enhanced protective properties, reflected by a higher impedance modulus and a broader phase-angle plateau. Following potentiostatic polarization, a continuous and dense passive film formed on the coating surface. XPS and TEM-EDS analyses identified the film as single phase Al_2O_3 with an amorphous structure and an average thickness of approximately 4.07 nm, effectively serving as a barrier against corrosive medium penetration. The growth kinetics of the film followed a high-field model, with thickness increasing logarithmically over polarization time, indicating that ion migration through the film is the rate-limiting step. Combined analysis using a point defect model reveals that the formation and growth of this passive layer are governed by both thermodynamic driving forces, namely the Al atom in Ti_3AlC_2 has lower vacancy formation energy and more negative Gibbs free energy of formation of Al_2O_3, and kinetic diffusion processes involving ion transport. This work elucidates the selective formation mechanism and growth kinetics of the Al_2O_3 passive film on Ti_3AlC_2 MAX phase coatings. The findings provide a theoretical foundation for understanding surface evolution of MAX phase materials

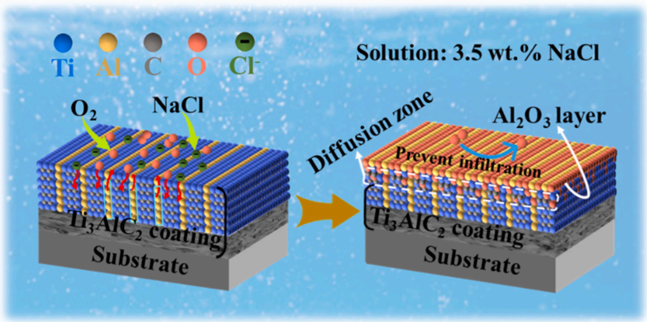

Fig. 11. Schematic diagram showing the passive mechanism of Ti_3AlC_2 coating in 3.5 wt.% NaCl solution.

in corrosive environments and offer critical insights for designing high performance corrosion resistance coating.

CRediT authorship contribution statement

Yuxi Xu: Writing – original draft, Resources, Methodology, Investigation, Data curation. **Qizhen He:** Visualization, Software, Data curation. **Guanshui Ma:** Writing – review & editing, Supervision, Investigation, Data curation. **Zhenyu Wang:** Writing – review & editing, Supervision, Resources, Project administration, Funding acquisition. **Kaihang Wang:** Validation, Methodology, Investigation. **Yiqun Feng:** Methodology, Investigation, Formal analysis, Data curation. **Aiying Wang:** Writing – review & editing, Supervision, Project administration, Funding acquisition, Conceptualization.

Declaration of competing interest

The authors declare that they have no known competing financial interests or personal relationships that could have appeared to influence the work reported in this paper.

Acknowledgments

This work was financially supported by the National Key R&D Program of China (2024YFB3816500), the National Science Fund for Distinguished Young Scholars of China (No.52025014), the National Natural Science Foundation of China (52571117), the Zhejiang Provincial Natural Science Foundation of China (No. LD24E010003). The Open Research Fund of the State Key Laboratory of Tropic Ocean Engineering Materials and Materials Evaluation (No. STOEM2025KF003).

References

[1] C. Ciszak, I. Popa, J.-M. Brossard, D. Monceau, S. Chevalier, NaCl induced corrosion of Ti-6Al-4V alloy at high temperature, Corros. Sci. 110 (2016) 91–104.
[2] M. Cao, L. Liu, Z. Yu, L. Fan, L. Ying, F. Wang, Studies on the corrosion behavior of Fe-20Cr alloy in NaCl solution spray at 600°C, Corros. Sci. 133 (2018) 165–177.
[3] L. Fan, L. Liu, Y. Cui, M. Cao, Z. Yu, E.E. Oguzie, Y. Li, F. Wang, Effect of streaming water vapor on the corrosion behavior of Ti60 alloy under a solid NaCl deposit in water vapor at 600°C, Corros. Sci. 160 (2019) 108177.
[4] H. Ding, Y. Li, M. Li, K. Chen, K. Liang, G. Chen, J. Lu, J. Palisaitis, P.O.Å. Persson, P. Eklund, L. Hultman, S. Du, Z. Chai, Y. Gogotsi, Q. Huang, Chemical scissor–mediated structural editing of layered transition metal carbides, Science 379 (2023) 1130–1135.
[5] M. Dahlqvist, M.W. Barsoum, J. Rosen, MAX phases – past, present, and future, Mater. Today 72 (2024) 1–24.
[6] S. Zhao, H. Xiao, Y. Li, Z. Zhang, Y. Wang, Q. Huang, L. Cao, F. Gao, C.L. Tracy, R. C. Ewing, C. Wang, Multi-stage phase transformation pathways in MAX phases, Nat. Commun. 16 (2025) 1554.
[7] K. Wang, Y. Zhang, G. Ma, Y. Xu, Z. Wang, A. Wang, Exceptional mechanical properties of $(Ti_{1-x}Zr_x)_2AlC$ MAX phase coatings with amorphous-nanocrystalline oxidation layers, J. Adv. Ceram. 15 (2025) 9221201.
[8] Y. Li, H. Kong, J. Yan, Q. Wang, X. Liu, M. Xiang, Y. Wang, Large-scale conformal synthesis of one-dimensional MAX phases, Nat. Commun. 15 (2024) 9275.
[9] G. Ma, A. Zhang, Z. Wang, K. Wang, J. Zhang, K. Xu, Y. Xu, S. Zhou, A. Wang, MAX phase coatings: synthesis, protective performance, and functional characteristics, Mater. Horiz. 12 (2025) 1689–1710.
[10] J. Cui, X. Hu, L. Zhang, Y. Yang, Y. Li, G. Chen, C. Tang, P. Ke, Highly efficient self-healing of fractured Ti_3AlC_2 MAX phase nanowires, Adv. Funct. Mater. 35 (2025) 2422697.
[11] J. Yuan, S. Zhou, H. Wu, Z. Wang, Y. Zhang, G. Zhou, G. Ma, P. Ke, A. Wang, Ultrahigh strength-ductility of nanocrystalline Cr_2AlC coating under micropillar compression, Scripta Mater. 235 (2023) 115594.
[12] Y. Zhang, S. Zhang, A. Zhang, G. Ma, K. Wang, Z. Wang, A. Wang, Breaking the trade-off of hardness–ductility in $(Cr_{1-x}Mo_x)_2AlC$ MAX phase coatings via a hierarchical structure, J. Adv. Ceram. 13 (2024) 1748–1758.
[13] K. Xu, S. Zhou, Z. Wang, X. Sun, K. Yang, K. Wang, A. Wang, P. Ke, Prism-plane-textured Cr_2AlC MAX-phase coatings with superior resistance to coupled thermal-salt-steam corrosion, Corros. Sci. 258 (2026) 113395.
[14] G. Ma, D. Zhang, P. Guo, H. Li, Y. Xin, Z. Wang, A. Wang, Phase orientation improved the corrosion resistance and conductivity of Cr_2AlC coatings for metal bipolar plates, J. Mater. Sci. Technol. 105 (2022) 36–44.
[15] Y. Zhang, A. Zhang, Z. Li, W. Zhenyu, P.-l. Ke, A. Wang, Electrochemical corrosion inhibition of Cr_2AlC MAX phase coatings via Mo solid solution: comprehensive experimental and simulation study, J. Phys. Chem. C 128 (2024) 3916–3923.
[16] W. Gao, D. Yang, Z. Zhao, H. Wang, Y. Fu, N. Huang, Effect of Ti_3SiC_2 concentration on corrosion resistance and ICR in bipolar plates composite ceramic coatings, Surf. Coating. Technol. 489 (2024) 131126.
[17] M. Zhu, R. Wang, C. Chen, H. Zhang, G. Zhang, Electrochemical study on the corrosion behavior of Ti_3SiC_2 in 3.5% NaCl solution, RSC Adv. 7 (2017) 12534–12540.
[18] Z. Li, Y. Zhang, K. Wang, Z. Wang, G. Ma, P. Ke, A. Wang, Highly dense passivation enhanced corrosion resistance of Ti_2AlC MAX phase coating in 3.5 wt.% NaCl solution, Corros. Sci. 228 (2024) 111820.
[19] X. Wang, Y. Zhou, Solid-liquid reaction synthesis and simultaneous densification of polycrystalline Ti_2AlC, Int. J. Mater. Res. 93 (2002) 66–71.
[20] X.H. Wang, Y.C. Zhou, Microstructure and properties of Ti_3AlC_2 prepared by the solid-liquid reaction synthesis and simultaneous in-situ hot pressing process, Acta Mater. 50 (2002) 3143–3151.
[21] L. Yao, C.-C. Zhu, J.-X. Jiang, B.-B. Zhou, Mechanical properties of Ti_3AlC_2 ceramics before and after heat treatment, Rare Met. 41 (2022) 2777–2782.
[22] S. Rui, Z. Chao, K. Dejun, Salt spray corrosion behavior and electrochemical performance of laser cladded Ni60- Ti_3AlC_2 composite coatings in 3.5% NaCl solution, Mater. Today Commun. 36 (2023) 106550.
[23] S. Rui, K. Dejun, Laser cladded Co08-x Ti_3AlC_2 coatings: microstructure, corrosive-wear and electrochemical corrosion, Mater. Today Commun. 39 (2024) 109354.
[24] J.L. Lu, N. Abbas, J.N. Tang, J. Tang, G.M. Zhu, Synthesis and characterization of conductive ceramic MAX-phase coatings for metal bipolar plates in simulated PEMFC environments, Corros. Sci. 158 (2019) 108106.
[25] H. Li, H. Cao, F. Liu, Y. Li, F. Qi, X. Ouyang, N. Zhao, Microstructure, mechanical and electrochemical properties of Ti_3AlC_2 coatings prepared by filtered cathode vacuum arc technology, J. Eur. Ceram. Soc. 42 (2022) 2073–2083.
[26] M. Zhu, R. Wang, C. Chen, H.B. Zhang, G.J. Zhang, Comparison of corrosion behavior of Ti_3SiC_2 and Ti_3AlC_2 in NaCl solutions with Ti, Ceram. Int. 43 (2017) 5708–5714.
[27] D. Li, Y. Liang, X. Liu, Y. Zhou, Corrosion behavior of Ti_3AlC_2 in NaOH and H2SO4, J. Eur. Ceram. Soc. 30 (2010) 3227–3234.
[28] Z. Li, G. Zhou, Z. Wang, J. Yuan, P. Ke, A. Wang, HiPIMS induced high-purity Ti_3AlC_2 MAX phase coating at low-temperature of 700°C, J. Eur. Ceram. Soc. 43 (2023) 4673–4683.
[29] G. Kresse, J. Furthmüller, Efficient iterative schemes for ab initio total-energy calculations using a plane-wave basis set, Phys. Rev. B 54 (1996) 11169–11186.
[30] P.E. Blöchl, Projector augmented-wave method, Phys. Rev. B 50 (1994) 17953–17979.
[31] J.P. Perdew, K. Burke, M. Ernzerhof, Generalized gradient approximation made simple, Phys. Rev. Lett. 77 (1996) 3865–3868.
[32] H.J. Monkhorst, J.D. Pack, Special points for Brillouin-zone integrations, Phys. Rev. B 13 (1976) 5188–5192.
[33] S.-G. Lee, K.J. Chang, Energetics and hydrogen passivation of carbon-related defects in InAs and $In_{0.5}Ga_{0.5}As$, Phys. Rev. B 53 (1996) 9784–9790.
[34] X.H. Wang, Y.C. Zhou, Layered machinable and electrically conductive Ti2AlC and Ti_3AlC_2 ceramics: a review, J. Mater. Sci. Technol. 26 (2010) 385–416.
[35] A.A. Hermas, M.S. Morad, A comparative study on the corrosion behaviour of 304 austenitic stainless steel in sulfamic and sulfuric acid solutions, Corros. Sci. 50 (2008) 2710–2717.
[36] X. Yang, A. Wolcott, G. Wang, A. Sobo, R.C. Fitzmorris, F. Qian, J.Z. Zhang, Y. Li, Nitrogen-doped ZnO nanowire arrays for photoelectrochemical water splitting, Nano Lett. 9 (2009) 2331–2336.
[37] J. Zhang, Y. Zhang, Z. Wang, G. Ma, A. Zhang, K.-R. Lee, A. Wang, Enhancing corrosion resistance of Ti_2AlC MAX phase through Sn solid solution in harsh acidic environments, Corros. Sci. 255 (2025) 113073.
[38] H. Lu, Study on disodium hydrogen phosphate and 2, 4-dimethylpyridine as corrosion inhibitor for Q235 steel in 3.5 wt% NaCl solution, Trans. Mater. Res. 1 (2025) 100127.
[39] Y.-F. Zhang, L.-Y. Chen, Z.-X. Wang, H.-Y. Yang, M. Bobrov, D. Oleksandr, Y. Liu, L.-C. Zhang, Distinctive transpassivation behavior and characteristics of passive films of laser powder bed fusion produced and annealed Ti-6Al-4V in Hank's solution, J. Mater. Res. Technol. 37 (2025) 3013–3027.
[40] S. Hao, X.-M. Wen, J. Cheng, X.-Y. Yao, W.-Y. Huang, R.-F. Li, L.-Y. Chen, Tailoring corrosion resistance of laser powder bed fusion produced Ti-6Al-4V via heat treatment at 700 °C in potential biomedical applications: microstructural evolution and electrochemical behavior, Met. Adv. 39 (2026) 83–94.
[41] Y.-H. Chu, L.-Y. Chen, B.-Y. Qin, W. Gao, F. Shang, H.-Y. Yang, L. Zhang, P. Qin, L.-C. Zhang, Unveiling the contribution of lactic acid to the passivation behavior of Ti-6Al-4V fabricated by laser powder bed fusion in Hank's solution, Acta Metall. Sin. 37 (2024) 102–118.
[42] A.M.M. dos Santos, R.J.C. Batista, L.A.M. Martins, M. Ilha, M.Q. Vieira, D. R. Miquita, F.C.R. Guma, I.L. Müller, T.M. Manhabosco, Corrosion and cell viability studies of graphite-like hydrogenated amorphous carbon films deposited on bare and nitrided titanium alloy, Corros. Sci. 82 (2014) 297–303.
[43] B. Ramírez Barat, E. Cano, In situ electrochemical impedance spectroscopy measurements and their interpretation for the diagnostic of metallic cultural heritage: a review, Chemelectrochem 5 (2018) 2698–2716.
[44] Y. Zhang, T. Zuo, Y. Cheng, P.K. Liaw, High-entropy alloys with high saturation magnetization, electrical resistivity and malleability, Sci. Rep. 3 (2013) 1455.
[45] K. Wang, J. Shen, D. Chen, Y. Dai, J. Lu, F. Gan, Q. Yao, Z. Lu, J. Wang, Effect of $Tb_{71.5}Fe_{28.5}$ additions on the microstructure and properties of recycled Nd-Fe-B magnets, Trans. Mater. Res. 1 (2025) 100142.
[46] C.O.A. Olsson, M.G. Vergé, D. Landolt, EQCM study of anodic film growth on valve metals, J. Electrochem. Soc. 151 (2004) B652.

[47] Y. Yin, H. Li, S. Pan, J. Zhang, Q. Han, S. Yang, Electrochemical behaviour of passivation film formed on SLM-fabricated Hastelloy X superalloy surface in 10 wt.% $NaNO_3$ solution, Corros. Sci. 206 (2022) 110494.

[48] C. Escrivà-Cerdán, E. Blasco-Tamarit, D.M. García-García, J. García-Antón, R. Akid, J. Walton, Effect of temperature on passive film formation of UNS N08031 Cr-Ni alloy in phosphoric acid contaminated with different aggressive anions, Electrochim. Acta 111 (2013) 552–561.

[49] L.-Å. Näslund, P.O.Å. Persson, J. Rosen, X-ray photoelectron spectroscopy of Ti_3AlC_2, $Ti_3C_2T_z$, and TiC provides evidence for the electrostatic interaction between laminated layers in MAX-phase materials, J. Phys. Chem. C 124 (2020) 27732–27742.

[50] W. Zhu, X. Li, C. Zheng, C. Zhang, Q. Mao, Y. Bi, Hydrothermal corrosion behavior of Ti_3SiC_2 MAX phase at atomic scale under simulated PWR conditions, Corros. Sci. 209 (2022) 110728.

[51] A. Zhang, K. Wang, Y. Zhang, G. Ma, W. Yang, G. Zhou, P. Ke, Z. Wang, A. Wang, Towards developing Ti_2AlC coatings with improved oxidation resistance via Nb solid solution, J. Alloys Compd. 1002 (2024) 175524.

[52] G.-q. Wang, N. Wang, Y.-t. Hu, J. Wang, C.-h. Gao, J. Wang, J.-j. Xue, K.-x. Yan, Corrosion resistance of self-healing three-dimensional Ti/Al-doped TiO_2 nanotubes Ti_3AlC_2 coating deposited by magnetron sputtered on copper, J. Cent. South Univ. 32 (2025) 867–881.

[53] H. Li, H. Cao, J. Yang, Y. Li, F. Qi, N. Zhao, X. Ouyang, Influence of annealing temperature on the structure and properties of Ti_3AlC_2 coatings by FCVA method, Mater. Char. 194 (2022) 112421.

[54] Y.-W. Cui, L.-Y. Chen, Y.-H. Chu, L. Zhang, R. Li, S. Lu, L. Wang, L.-C. Zhang, Metastable pitting corrosion behavior and characteristics of passive film of laser powder bed fusion produced Ti-6Al-4V in NaCl solutions with different concentrations, Corros. Sci. 215 (2023) 111017.

[55] M. Gao, S. Zhang, B. Yang, J. Wang, Influence of yttrium on surface chemistry and stability of passive film in Al-based binary metallic glasses, Appl. Surf. Sci. 457 (2018) 536–547.

[56] Y.-W. Cui, L.-Y. Chen, P. Qin, R. Li, Q. Zang, J. Peng, L. Zhang, S. Lu, L. Wang, L.-C. Zhang, Metastable pitting corrosion behavior of laser powder bed fusion produced Ti-6Al-4V in Hank's solution, Corros. Sci. 203 (2022) 110333.

[57] M.J. Carmezim, A.M. Simões, M.F. Montemor, M.D. Cunha Belo, Capacitance behaviour of passive films on ferritic and austenitic stainless steel, Corros. Sci. 47 (2005) 581–591.

[58] M. Chen, Z. Jia, Z. Wang, C. Xiang, J. Pu, G. Sun, E.-H. Han, Insights into the passivity and electrochemistry of CoCrFeMnNi high entropy alloy fabricated by underwater laser direct metal deposition, Corros. Sci. 237 (2024) 112289.

[59] C.H. Hsu, F. Mansfeld, Technical note: concerning the conversion of the constant phase element parameter Y0 into a capacitance, Corrosion 57 (2001) 747–748.

[60] E. Sikora, D.D. Macdonald, Defining the passive state, Solid State Ionics 94 (1997) 141–150.

[61] B.N. Popov, Chapter 4 – Passivity (2015) 144–179.

[62] D.D. Macdonald, The point defect model for the passive state, J. Electrochem. Soc. 139 (1992) 3434.

[63] H. Wang, H. Han, G. Yin, C.-Y. Wang, Y.-Y. Hou, J. Tang, J.-X. Dai, C.-L. Ren, W. Zhang, P. Huai, First-principles study of vacancies in Ti_3SiC_2 and Ti_3AlC_2, Materials 10 (2017) 103.

[64] I. Barin, ThO-Tm_2O_3, in: Thermochemical Data of Pure Substances, 1995, pp. 1656–1724.

[65] I. Barin, Examples of thermodynamic calculations, in: Thermochemical Data of Pure Substances, 1995, pp. 41–58.

[66] A.H. Heuer, Oxygen and aluminum diffusion in α-Al_2O_3: how much do we really understand? J. Eur. Ceram. Soc. 28 (2008) 1495–1507.